A Correction Algorithm for Rotor-Induced Airflow and Flight Attitude Changes during Three-Dimensional Wind Speed Measurements Made from A Rotary Unmanned Aerial Vehicle

Yanrong Yang[1+], Yuheng Zhang[1+], Tianran Han[1], Conghui Xie[2], Yayong Liu[2], Yufei Huang[1], Jietao Zhou[1], Haijiong Sun[1], Delong Zhao[3], Kui Zhang[4], Shao-Meng Li[1*]

[1]College of Environmental Sciences and Engineering, Peking University, Beijing 100871, China

[2]Laboratory of Gas Instrument Testing, Center for Environmental Metrology, National Institute of Metrology, Beijing 100029, China

[3]Beijing Weather Modification Center, Beijing 100089, China

[4]Beijing Wisdominc Technology Co., Ltd, Beijing 100070, China

+Contributed equally to the work

Correspondence to: Shao-Meng Li (shaomeng.li@pku.edu.cn)

Abstract. A hexacopter unmanned aerial vehicle (UAV) was fitted with a three-dimensional sonic anemometer to measure three-dimensional wind speed. To obtain accurate results for three-dimensional wind speeds, we developed an algorithm to correct biases caused by the rotor-induced airflow disturbance, UVA movement, and attitude changes in the three-dimensional wind measurements. The wind measurement platform was built based on a custom-designed integration kit that couples seamlessly to the UAV, equipped with a payload and the sonic anemometer. Based on an accurate digital model of the integrated UAV-payload-anemometer platform, computational fluid dynamics (CFD) simulations were performed to quantify the wind speed disturbances caused by the rotation of the UAV's rotor on the anemometer during the UAV's steady flight under headwind, tailwind, and crosswind conditions. Through analysis of the simulated data, regression equations were developed to predict the wind speed disturbance, and the correction algorithm for rotor disturbances, motions, and attitude changes was developed. To validate the correction algorithm, we conducted a comparison study in which the integrated UAV flew around a meteorological tower on which three-dimensional wind measurements were made at multiple altitudes. The comparison between the corrected UAV wind data and those from the meteorological tower demonstrated an excellent agreement. The corrections result in significant reductions in wind speed bias caused mostly by the rotors, along with notable changes in the dominant wind direction and wind speed in the original data. The algorithm enables reliable and accurate wind

speed measurements in the atmospheric boundary layer made from rotorcraft UAVs.

Keywords: UAV; Rotor Disturbance; Three-dimensional Wind; Correction Algorithm

1 Introduction

Wind measurement is crucial in various fields of research and application, including meteorology and environmental sciences. Accurate wind characteristics facilitate modeling of atmospheric transport patterns (Gryning et al., 1987; Stockie, 2011), remote sensing data verification (Drob et al., 2015), model input data assimilation (Gousseau et al., 2011; Vardoulakis et al., 2003) and digital modeling result optimization (Booij et al., 1999; Van Hooff and Blocken, 2010). In particular, wind profile measurements near surface can improve the understanding of atmospheric boundary layer (ABL) dynamics and micrometeorological turbulence at the surface (Seibert et al., 2000), allowing detailed understandings and model description of energy and mass exchanges between air and surfaces and transport processes.

The recent development of unmanned aerial vehicles (UAVs) has provided an opportunity for the measurement of wind fields in three dimensions with high spatial resolutions (Mcgonigle et al., 2008; Martin et al., 2011; Kim and Kwon, 2019). The small size, low flight altitude, high mobility and ability to assemble sensing devices make UAVs ideal platforms from which to measure wind in the ABL (Thielicke et al., 2021; Shaw et al., 2021; Stewart et al., 2021). Multirotor UAVs allow flexible control of flight attitude and stationary hovering, and can carry varying payloads depending on the number of rotors (Villa et al., 2016; Riddell, 2014; Bonin et al., 2013; Stewart et al., 2021), offering significant advantages in capturing high-resolution wind characteristics in low-altitude conditions (Anderson and Gaston, 2013; Mcgonigle et al., 2008).

UAVs are often employed to measure wind characteristics both directly and indirectly. Indirect measurement methods involve utilizing pre-installed sensors on the UAV (Elston et al., 2015), in conjunction with specialized flight patterns and wind retrieval algorithm (Bonin et al., 2013; Rautenberg et al., 2018; Gonzalez-Rocha et al., 2019) to achieve wind speed measurement. While these methods offer advantages of operational simplicity and cost-effectiveness, their core principle relies on inversely estimating wind speed through dynamic parameters such as thrust, attitude angles, and flight velocity (Crowe et al., 2020; Donnell et al., 2018; Sikkel et al., 2016; Simma et al., 2020). However, their accuracy is critically dependent on both the measurement precision of inertial measurement unit (IMU)

and the computational reliability of inversion algorithms. Specifically, inherent noise interference in IMU sensors (e.g., gyroscope's angular rates can be severely affected by external disturbances up to 0.5 °/s) (Hoang et al., 2021; Neumann and Bartholmai, 2015), combined with uncertainties in parameter configuration within inversion algorithms (the root mean squared errors (RMSE) of wind speed estimation is 1-1.4) (Bonin et al., 2013), can lead to significant deviations in wind speed estimations. Furthermore, these methods typically assume constant aerodynamic parameters for UAVs, an assumption that often fails to hold in practical complex wind field environments (Bonin et al., 2013).

In contrast, direct measurement methods entail installing additional wind sensors on the UAV to obtain real-time wind information in the field. Porous probes (Soddell et al., 2004; Spiess et al., 2007), pitot tubes (Niedzielski et al., 2017; Langelaan et al., 2011), and anemometers (Rogers and Finn, 2013; Nolan et al., 2018) are commonly used sensors. Sonic anemometers are a more prevalent choice for rotorcraft UAVs, capable of measuring wind speed by detecting changes in the speed of sound travel between different sensors (Thielicke et al., 2021). Recent experiments have demonstrated that under highly turbulent conditions, UAV equipped with properly installed sonic anemometers in wind tunnels can achieve wind speed measurements with RMSE ranging from 4.3% to 15.5% compared to bistatic lidar (Thielicke et al., 2020). Due to the increasing use of rotorcraft UAVs for wind measurements, sonic anemometers are recognized as one of the most promising methods in terms of measurement accuracy and precision.

Sonic anemometers have been mounted onto rotary-wing UAVs for measuring wind speed to varying degrees of success. Typically, an anemometer is mounted at a position along the central axis above the UAV, with data adjusted for the additional wind speed signals induced by UAV motion and attitude changes. Nevertheless, the strong airflow perturbations caused by the rotating propellers can distort real wind flow patterns and significantly affect the accuracy of wind measurements (De Divitiis, 2003). However, these distortions were not considered in the adjustment algorithms. To address this issue, researchers have developed several new correction methods. The first method involves mounting the anemometer along the central axis high above the UAV where the rotor wash effects are believed to be limited on the wind speed measurement (Shimura et al., 2018; Barbieri et al., 2019). Johansen concluded that anemometers at about 40 to 45 mm above the multi-rotor plane of small UAV the flow influences from rotors are negligible (Johansen et al., 2015). However, it may not be suitable for

88 hexacopters and octocopters due to the high position required, which may raise safety and flight control

89 concerns. The second method involves new corrections based on experiments in an indoor area to

90 measure wind velocity signal bias caused by the rotors during flight and then subtracting the bias

91 (Palomaki et al., 2017). Palomaki et al. (2017) quantified rotor-induced wind speed errors as 0.5 m/s

92 compared to tower-mounted anemometers and subtracted these errors from the directly measured wind

93 speed values in subsequent analyses (Palomaki et al., 2017). However, this method is limited by the size

94 of the indoor area, inadequate for full simulations of real UAV rotor speed and attitude changes during

95 flight, and insufficient for the development of a comprehensive correction scheme. Additionally, it does

96 not take into account the detailed coupling of true winds with propeller downwash. The third method is

97 similar to the second except the use of wind tunnels to establish a more accurate relationship between

98 increased air speed and UAV motion or attitude parameters (Thielicke et al., 2021; Neumann and

99 Bartholmai, 2015). While effective in determining numerical relationships, the method is limited by the

100 high cost of wind tunnel experiments (Dao et al., 2023), and more importantly, by the additional errors

101 introduced by reflected airflows from the wind tunnel walls and ground (Haleem, 2021; Pettersson and

102 Rizzi, 2008), as well as the same issues of full simulations of real UAV rotor speed and attitude changes

103 during flight.

104 The flaws in these correction methods could be addressed by using computational fluid dynamics

105 (CFD) simulations to analyze the airflow generated by the UAV's propellers. As far as we know, CFD

106 has been employed to analyze airflow patterns around drones but hasn't been utilized to correct wind

107 measurements obtained from UAVs (Oktay and Eraslan, 2020; Hedworth et al., 2022). In this paper, we

108 introduce a three-dimensional wind speed correction algorithm for sonic anemometer wind

109 measurements taken from a rotary UAV. This algorithm considers the rotor-induced airflow of the UAV,

110 based on CFD simulations, along with the UAV's motion and attitude changes during flight. The

111 accuracy of the algorithm is confirmed by comparing the corrected wind speeds with those measured

112 from a meteorological tower at multiple altitudes. These results could contribute to ongoing efforts

113 aimed at enhancing the performance and reliability of UAV-based wind speed measurement techniques.

114 Additionally, they pave the way for potential applications, such as quantifying pollutant emissions from

115 industrial complexes (Han et al., 2023).

2 Method

2.1 Digital Model Representation and Simulation Tool

2.1.1 Digital Model Representation

A six-rotor UAV (KWT-X6L-15, ALLTECH, China), equipped with six 32 cm diameter propellers driven by M10 KV100 brushless DC motors, was the platform from which wind was measured. The UAV has a symmetrical motor wheelbase of 1765 mm with an unloaded takeoff weight of 22.5 kg and a maximum flight speed of 18 m s^{-1}. It has a flight endurance > 30 min while carrying its maximum payload of 15 kg.

A miniature three-dimensional ultrasonic anemometer (Trisonica-Mini Wind and Weather Sensor, Anemoment, America) allowed the measurement of wind speed under 15 m s^{-1} with an accuracy of $\pm$ 0.1 m s^{-1} and a resolution of 0.1 m s^{-1}, and wind direction of 0 - 360° with an accuracy of $\pm$ 0.1° and a resolution of 0.1°. It was set at 70 cm above the plane of the propellers of the UAV, mounted on a custom-design carbon fiber tube and frame which was further mounted onto a rectangular carbon fiber support base attached to the underbelly of the UAV body, to minimize the effect of propellers-induced flow on the anemometer measurement. The x_t-y_t-z_t coordinate axes of the anemometer, with its center as the origin, were set to be parallel to the x-y-z axes of the aircraft body frame. The mounting of the three-dimensional anemometer is shown in Fig. 1(a).

A base digital model of the UAV was provided by its manufacturer for the present CFD simulations. The digital model was further augmented with the accurate digital representation of the three-dimensional anemometer and its mounting frame. Furthermore, considering that the UAV wind measurements are usually tied to other air measurement applications, necessitating additional payload attached to the UAV underbelly simultaneously. Such a payload on the UAV needs also to be included in the digital model for the CFD simulation. In the present case, we added the digital model of a 6.37 kg air sampler developed in our group (Yang et al., 2024) to the UAV base digital model (Fig. 1(b)).
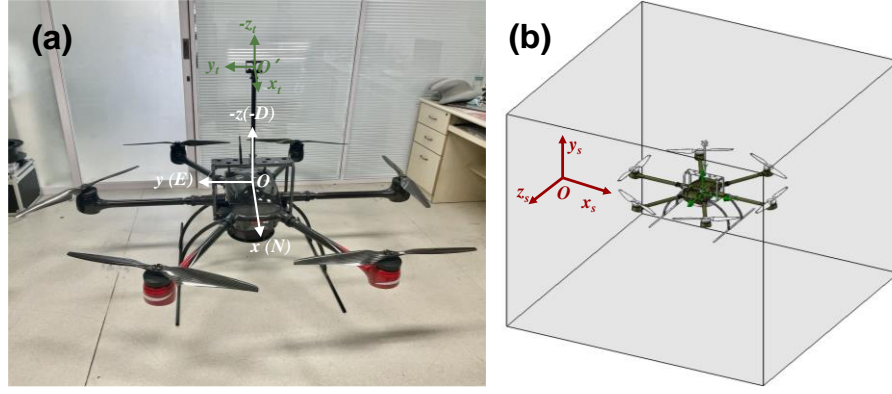
Figure 1: The establishment of the coordinate system and numerical simulation model for the UAV wind measurement platform. (a) The UAV wind speed measurement platform. (b) The digital model of the UAV wind measurement platform in the 3D CFD model simulation domain.

2.1.2 Simulation Tool

The CFD simulations were conducted using SolidWorks Flow Simulation 2022, a pressure-based finite volume solver employing a fully coupled turbulence modeling approach. It employs an adaptive Cartesian mesh approach for three-dimensional solid meshing, with the governing equations being the Navier-Stokes equations for simulating the interaction of fluids, and the turbulence model utilizing the standard k-ε two-equation model (Jonuskaite, 2017).

The selection of SolidWorks Flow Simulation was driven by its seamless integration with CAD geometries, which eliminated potential errors associated with STL file conversions for our complex multi-rotor UAV design. Additionally, its wall functions for boundary layers effectively resolve gradient variations in boundary layers around rotating blades, reducing trial and error related to near-wall settings. The built-in solver convergence adopts a phased approach to multiple variant scenarios, decreasing the need for re-runs caused by insufficient convergence and thereby conserving computational costs. Its unique turbulence model automatically determines flow regimes (laminar, transitional, and turbulent), ensuring shorter turbulence model setup times while maintaining enhanced model accuracy (Azmi et al., 2017; Ramya et al., 2015).

While ANSYS Fluent offers advanced transient turbulence models (e.g., DES/LES), its computational cost for equivalent spatial resolution was typically higher than SolidWorks (Afaq and Ahmad, 2023). Given our need to simulate over 100 operational scenarios, SolidWorks' balance of engineering accuracy and computational tractability was deemed optimal for deriving empirical correction algorithm.

For CFD simulations, the complete digital model for the UAV and its payloads was set in the x_s-y_s-z_s simulation coordinate system in Solidworks, on a one-to-one scale (Fig. 1(b)).

2.2 Simulation Scenarios

For the UAV flight simulation, we considered over a hundred flight envelope scenarios, including parameters such as UAV flight altitude, wind direction, and wind speed. Since the UAV's predominant flights are within the atmospheric boundary layer, characterized by significant variability in wind speed and directions, a flight envelope for the UAV in the simulated environments was setup for the complete UAV digital model for flight altitudes of 30 and 1000 meters, respectively. The lower height (30 m) represents the typical operational altitude for industrial UAV applications within the boundary layer, while the upper height (1000 m) corresponds to the altitude where atmospheric flow transitions to more stable, low-density free-stream conditions. These flight envelopes were designed for the UAV to subject to headwind, tailwind, and crosswind relative to its flight direction. Under the constraint that the UAV can only operate under true wind speeds ≤ 18 m s^{-1}, and assuming the applicability of the correction algorithm to most flight scenarios, CFD simulations were conducted for the UAV under these three wind directions. The simulations encompassed the following flight envelopes as listed in Table 1: the UAV flew at ground speeds of 18, 14, 10, and 8 m s^{-1}, respectively, and adapted to wind speeds of 1.5, 3.3, 5.4, 7.9, 10.7, and 14 m s^{-1}. It should be noted that the numerical simulations were conducted by converting wind speed and ground speed into airspeed through vector synthesis.

Table 1: The simulation flight envelope scenarios for the UAV-based wind measurement platform.

Wind Type	Ground Speed (m s^{-1})	Wind speed (m s^{-1})	Wind Type	Ground Speed (m s^{-1})	Wind speed (m s^{-1})	Wind Type	Ground Speed (m s^{-1})	Wind speed (m s^{-1})
	8	1.5		8	1.5		8	1.5
		3.3			3.3			3.3
		5.4			5.4			5.4
		7.9						7.9
		10.7						10.7
Tailwind			Headwind			Crosswind		14
	10	1.5		10	1.5		10	1.5
		3.3			3.3			3.3
		5.4			5.4			5.4
		7.9			7.9			7.9
		10.7						10.7

					14
	1.5		1.5		1.5
	3.3		3.3		3.3
14	5.4	14	5.4	14	5.4
	7.9		7.9		7.9
	10.7		10.7		10.7
					14
	1.5		1.5		1.5
	3.3		3.3		3.3
18	5.4	18	5.4	18	5.4
	7.9		7.9		7.9
	10.7		10.7		10.7
			14		14

2.3 Flight Parameters

The movements of the UAV through air, including takeoff, ascent/descent, attitude changes, turning, and horizontal flights, are driven by the rotary propellers, whose power requirement is closely tied to the weights of the UAV and its payload as well as the relative motions of the UAV in air. During a normal flight, the UAV adjusts its inclination angle and propeller speeds in order to achieve a set ground speed for flight. By analyzing the gravity G, pull T and wind resistance D experienced by the UAV under flight conditions (Fig. 2), its inclination angle θ and propeller rotation speed M can be calculated according to Eqs. (1) - (5) (Quan, 2017).
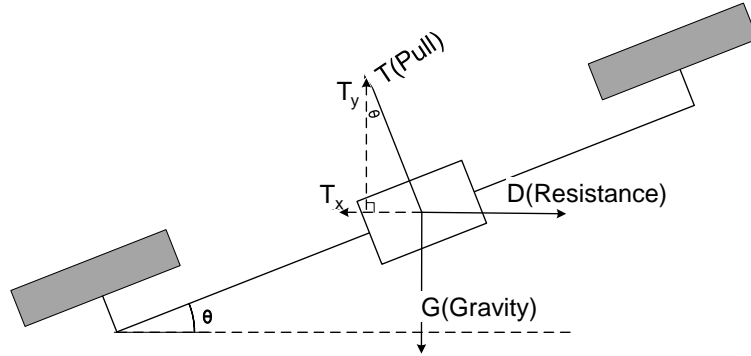

Figure 2: Schematic diagram of forces acting on a UAV.

$$\tan\theta \times mg = D, \tag{1}$$

$$p \times (\sin\theta \times S_{xoy} + \cos\theta \times S_{xoz}) = D, \tag{2}$$

$$0.5\rho(V_{wind} + V_{UAV})^2 = p, \tag{3}$$

$$\cos\theta \times mg = T, \tag{4}$$

$$T = C_T \times \rho \times \left(\frac{M}{60}\right)^2 \times D_p^{\ 4}, \tag{5}$$

where θ is the inclination angle of the UAV; m is the combined weight of the UAV and the payloads (i.e, the air sampler and the anemometer along with its installation frame in the present case), calculated to be 28.869 kg; g is the gravitational constant at 9.8 m s^{-2}; D is the wind resistance in Newtons; V_{wind} is the wind speed in m s^{-1}; V_{UAV} is the ground speed of the UAV in m s^{-1}; p is the wind pressure on the UAV in N/m^2; S_{xoy} and S_{xoz} are the projected surfaces of the UAV in the horizontal direction and vertical directions, determined to be 0.296 and 0.229 m^2, respectively; C_T is the rotor pull coefficient with an experimentally determined value of 0.048542; D_p is the UAV propeller diameter at 0.8128 m; ρ is the air density in kg m^{-3}; T is each rotor pull in Newton; M is the rotation speed of the rotors in RPM.

The complete flight envelope was defined by combinations of critical parameters, including wind directions, wind speeds, airspeeds, ground speed, inclination, wind resistance, pull, and M. A series of CFD simulations were conducted to systematically evaluate the simulated wind field characteristics for each unique parameter set within this envelope.

2.4 Simulation Parameters

The simulation parameters primarily include the computational domain and mesh, fluid and environmental properties, as well as the rotating region. During the CFD flow simulations of the UAV using Solidworks, the computational domain dimensions (3.3 × 3.3 × 3.3 m³) were determined by prioritizing the analysis of flow field distribution around the anemometer while balancing computational costs. The computational domain was divided into two parts with different spatial resolutions based on the grid sizes，considering the computational time and accuracy required for resolving the details of the digital UAV model. The first part was the global domain with a grid size of 0.23 × 0.23 × 0.23 m³, providing a lower spatial resolution. The second part was a nested subdomain within the global domain, specifically defined for the position and dimensions of the anemometer to simulate the measured velocities. The grid size for this nested subdomain was set at 0.0125 × 0.0125 × 0.0125 m³, providing a higher spatial resolution. The total number of grids in the computational domain was 1.11×10^8, and the specific grid configurations are shown in Fig. 3. The wall is set as an adiabatic wall, and its roughness is set to 0. The fluid was modeled as air with characteristics of turbulent and laminar flow. To isolate the rotor-induced flow dynamics from background atmospheric turbulence, a turbulence intensity of 0.1% and a turbulence length scale of 0.012 m were set. This low turbulence intensity minimizes confounding effects from ambient atmospheric fluctuations, while the length scale corresponds to the anemometer

227 frame width (~0.01 m) to resolve rotor-generated eddies. These assumptions prioritize the systematic

228 bias correction for rotor-induced airflow. The atmospheric pressure was adjusted to 1.01×10^5 and 9.00

229 $\times 10^4$ Pa at altitudes of 30 m and 1000 m, respectively, and the atmospheric temperature was assumed

230 to be 25 °C at both altitudes. The relative humidity at different altitudes was determined based on the

231 prescribed pressure and temperature corresponding to each altitude. The detailed configurations of these

232 parameters are listed in Table 2.

233　　The UAV's airspeed and aerodynamic angles were configured according to the different flight

234 parameters described in Sect. 2.2 and 2.3. To represent the rotor digitally, six virtual cylinders of the

235 same volume were used to encapsulate the six rotors, with their circumferences match the rotating

236 trajectory of the propeller tip. These virtual cylinders were treated as the rotational regions in the CFD

237 simulation, with their rotation directions aligned with the actual rotation direction of the UAV's

238 propellers. The rotation direction from rotor No. 1 to 6 was alternately clockwise and counterclockwise,

239 and the rotation speed for each flight condition was obtained from Eqs. (1) - (5).
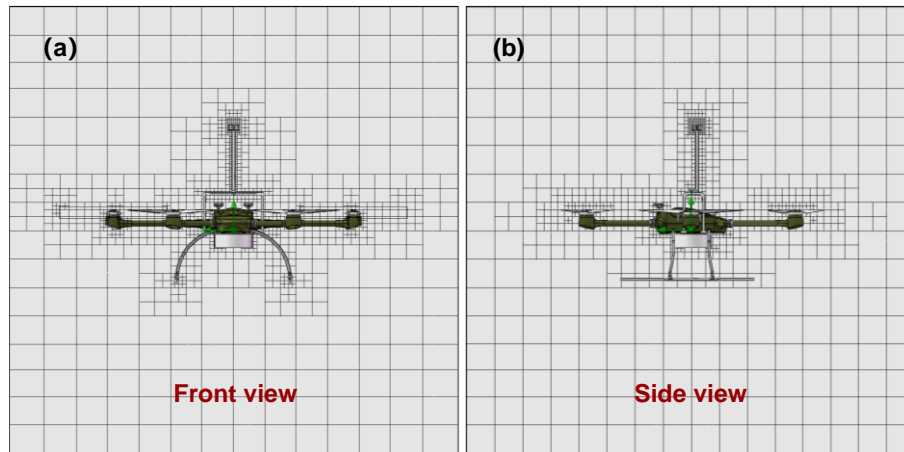
240
241 **Figure 3：Grid configuration of the computational domain.**

242 **Table 2：Simulation parameters configuration.**

Parameters	Content
Computational domain size	$3.3 \times 3.3 \times 3.3$ m³
Global domain grid size	$0.23 \times 0.23 \times 0.23$ m³
Subdomain grid size	$0.0125 \times 0.0125 \times 0.0125$ m³
Total number of computational domain grids	1.11×10^8
Turbulence intensity	0.1%
Turbulence length scale	0.012 m
Roughness	0
30 m atmospheric pressure	1.01×10^5 Pa
1000 m atmospheric pressure	9.00×10^4 Pa

| 30 m atmospheric temperature | 25 °C |
| 1000 m atmospheric temperature | 25 °C |

243   To ensure relatively accurate simulations, two categories of flow field properties were specified as

244   computational objectives prior to the start of the simulations, and the simulations were terminated upon

245   convergence of the simulation results for all objectives. The first category comprised global domain

246   computational objectives, including average total pressure (P_G), average velocity (V_G), average vertical

247   velocity (V_{Gy}), and average forward velocity (V_{Gz}), where the subscript G denotes the global domain.

248   The second category consisted of subdomain computational objectives, which included the average

249   velocity (V_S), three-dimensional average speed components V_{Sx}, V_{Sy} and V_{Sz} at the anemometer position

250   in the simulation coordinate system. It is noteworthy that the aforementioned average values refer to the

251   spatial averages over the global domain or subdomain.

252   Upon simulation completion, these velocity components (V_{Sx}, V_{Sy}, V_{Sz}) were further converted to

253   velocity components at the anemometer sensor position (u_{x_sensor}, u_{y_sensor}, u_{z_sensor}) in the airframe

254   coordinate according to the coordinate system shown in Fig. 1((a) and (b)) and Eqs. (6) - (8) below. The

255   converted velocities, u_{x_sensor}, u_{z_sensor}, u_{z_sensor}, were subtracted from the airspeed (denoted as u_{x_air},

256   u_{y_air}, and u_{z_air}) setting for each CFD simulation, to estimate the false wind signals arising from the

257   induced flow by the UAV rotors, expressed with Δu_x, Δu_y and Δu_z, respectively, using Eqs. (9) - (11).

258    $$u_{x\_sensor} = -Vs_z, \tag{6}$$

259    $$u_{y\_sensor} = Vs_x, \tag{7}$$

260    $$u_{z\_sensor} = -Vs_y, \tag{8}$$

261    $$\Delta u_x = u_{x\_sensor} - u_{x\_air}, \tag{9}$$

262    $$\Delta u_y = u_{y\_sensor} - u_{y\_air}, \tag{10}$$

263    $$\Delta u_z = u_{z\_sensor} - u_{z\_air}, \tag{11}$$

264   In other words, the false wind signals Δu_x, Δu_y and Δu_z are the terms that must be determined and

265   corrected for in the wind measurements from the UAV.

266   **3 Result and Discussion**

267   **3.1 Example Analysis of Simulation Results**

268   According to the Sect. 2.2, this study develops a series of simulation scenarios for the UAV digital

269   model under various combinations of altitude (30 and 1000 m), wind direction (tailwind, headwind, and

270   crosswind), ground speed (8 to 18 m/s), and wind speed (1.5 to 14 m/s). To demonstrate the flow field

271   characteristics around the UAV under various scenarios, one UAV hovering scenario and six

272   representative simulation scenarios were specifically selected for analysis as examples.

273   Fig. 4 presents the cross-sectional view of the velocity flow field around the UAV in a hovering

274   state under wind-free conditions. In this scenario, the surrounding velocity field is solely generated by

275   the rotational induced flow from the UAV's own rotors. The simulated 2-4 m/s airflow around the

276   anemometer originates exclusively from rotor rotation, demonstrating that the rotor-induced flow during

277   hovering inherently interferes with wind speed measurements by the anemometer.


278
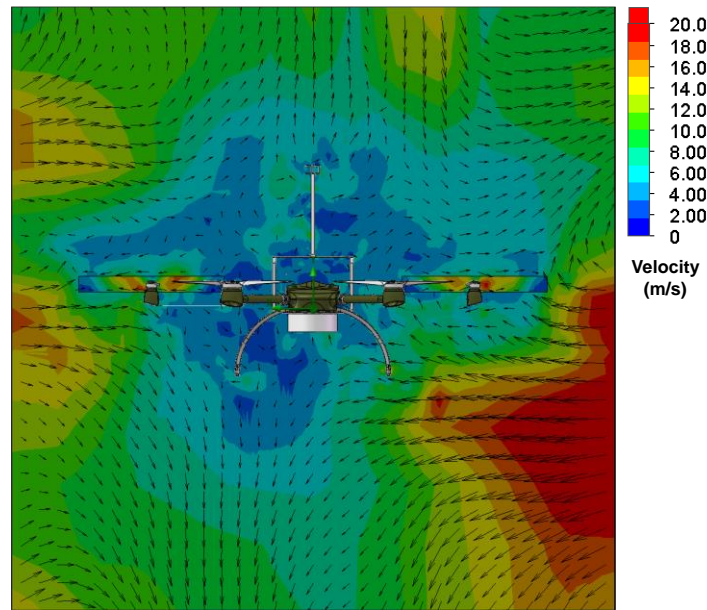
279 **Figure 4: The velocity flow field distribution of the UAV's hovering state.**

280   The other six scenarios include UAV flight simulations at altitudes of 30 m and 1000 m, with a

281   ground speed of 8 m/s and a wind speed of 5.4 m/s, under tailwind, headwind, and crosswind conditions.

282   Fig. 5 to 7 present cross-sectional views of the surrounding flow fields during UAV flight under these

283   conditions. In the figures, color gradients represent the magnitude of the velocity, while arrows indicate

284   both the direction and magnitude of the velocity. Overall, under varying wind conditions, the direction

285   and speed of airflow around the UAV show significant differences. While the airflow direction around

286   the UAV remains relatively consistent at the both simulation altitudes, the airflow speed at 1000 m is

287   slightly higher than at 30 m, particularly under tailwind conditions. Specifically, based on the ground

288   speed, wind direction, and wind speed settings, the UAV's airspeed relative to the wind is 2.6 m/s, 13.4

289   m/s, and 5.4 m/s in tailwind, headwind, and crosswind scenarios, respectively.

As show in Fig. 5 (a) and (b), in the tailwind scenario, the maximum downwash velocity occurs directly beneath the UAV rotors, with the airflow directed vertically downward. The next highest velocities are observed around the sides and above the rotors, where the airflow follows an inward and downward trend. The wind speed at the anemometer location is minimally influenced by the UAV rotors, meaning the measured wind speed represents the true airspeed. In the headwind scenario (Fig. 6 (a) and (b)), the highest airflow velocity is detected near the area directly above the rotors, with the airflow also following an inward and downward pattern. The lowest velocity is found directly below the rotors, where the airflow moves upward and outward. At the anemometer's location, some interference from the UAV rotors is present, so the wind speed at this point is a combination of the true airspeed and the rotor-induced velocity. As exhibited in Fig. 7 (a) and (b), in the crosswind scenario with wind blowing from left to right, the airflow around the UAV resembles that in the headwind scenario, but the overall flow field is deflected to the right due to the crosswind, with relatively lower airflow velocity. In the scenario with wind blowing from right to left, the flow field shifts to the left.

These simulation results show that the flow field around the UAV varies significantly depending on both the presence/absence of wind and its directional characteristics, and the anemometer experiences different levels of interference accordingly. Thus, accurately quantifying the interference of the UAV rotors on the anemometer is essential. However, in practical application scenarios, it is also necessary to comprehensively consider additional airflow disturbances induced by the UAV's own motion and attitude fluctuations, and to develop corresponding dynamic compensation algorithms.
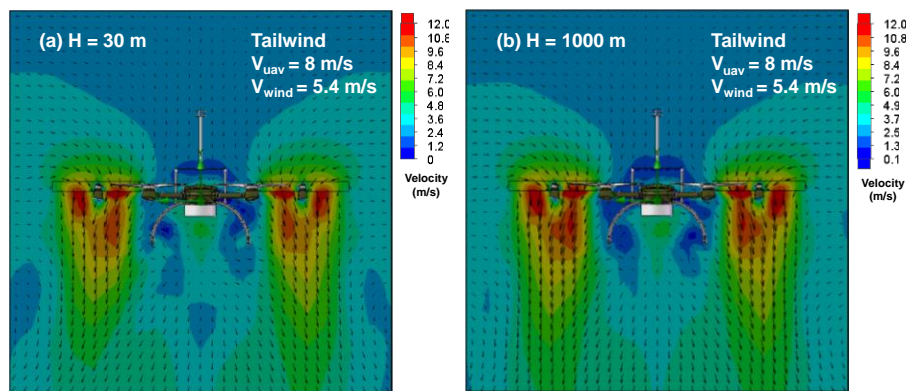
Figure 5: Simulation flow field example results of the UAV wind measurement platform in the tailwind scenario. (a) and (b) represent the longitudinal cross-sections of the simulation flow fields for the UAV at altitudes of 30 m and 1000 m, with a ground speed of 8 m/s and a wind speed of 5.4 m/s.
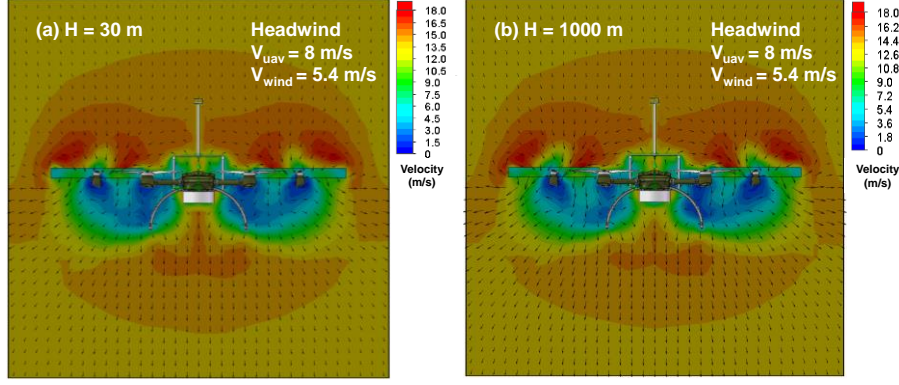
Figure 6： **Simulation flow field example results of the UAV wind measurement platform in the headwind scenario. (a) and (b) represent the longitudinal cross-sections of the simulation flow fields for the UAV at altitudes of 30 m and 1000 m, with a ground speed of 8 m/s and a wind speed of 5.4 m/s.**
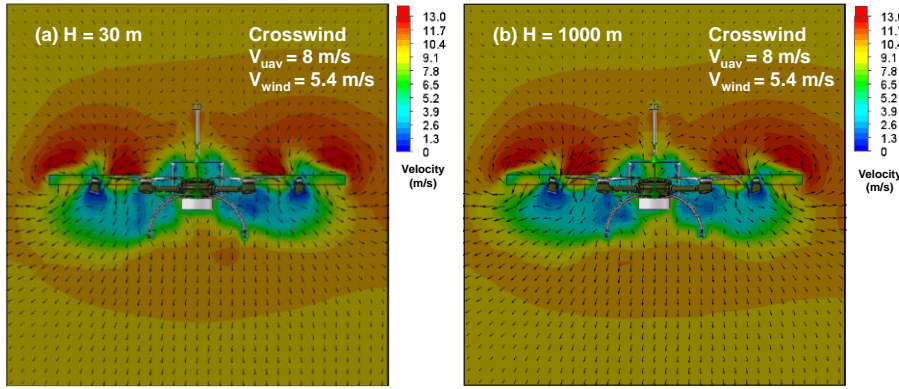
Figure 7： **Simulation flow field example results of the UAV wind measurement platform in the crosswind scenario. (a) and (b) represent the longitudinal cross-sections of the simulation flow fields for the UAV at altitudes of 30 m and 1000 m, with a ground speed of 8 m/s and a wind speed of 5.4 m/s.**

3.2 The effect of flight altitude on rotor interference with anemometer measurements

Through simulating the flight of UAV in all simulation scenarios, the false signals produced by the UAV rotors on the anemometer at different altitudes and wind characteristics were captured. Initially, the influence of flight altitude on the false signals was examined.

The simulated flight data under tailwind and headwind conditions were integrated into a unified data set since the UAV flight velocity vector is parallel to the tailwind and headwind velocity vectors during normal flight. The simulated false wind signals on the anemometer in the airframe x, y, and z directions, caused by the propeller induced airflow under tailwind and headwind conditions, were represented by $\Delta u_x^{\mathrm{T/HW}}$, $\Delta u_y^{\mathrm{T/HW}}$, and $\Delta u_z^{\mathrm{T/HW}}$, respectively. For the tailwind and headwind datasets, according to the Wilcoxon non-parametric test for paired samples, as shown in Table 3, the differences in $\Delta u_x^{\mathrm{T/HW}}$, $\Delta u_y^{\mathrm{T/HW}}$ and $\Delta u_z^{\mathrm{T/HW}}$ were not significant ($p < 0.05$) at either the 30 m or the 1000 m

14

altitudes. Therefore, in the presence of tailwind or headwind, the interference from the UAV propeller-induced flow on the anemometer measurement can be considered independent of the flight altitude in this altitude range.

Similarly, the simulated false wind signals for the crosswind conditions on the anemometer in the x, y, and z directions were represented by Δu_x^{CW}, Δu_y^{CW}, and Δu_z^{CW}. The Wilcoxon non-parametric test of paired samples was also applied (shown in Table 1) between the two altitudes. No significant differences were found for Δu_x^{CW}, Δu_z^{CW} between the two altitudes, but there was an obvious discrepancy for Δu_y^{CW}（$p = 0.00$）at the two altitudes. This indicates that under cross wind conditions, the disturbances of the UAV propeller in the x and z directions of the anemometer are not altitude dependent, but that in the y direction it is necessary to distinguish the altitude. This behavior can be attributed to differences in the interaction between the y direction component and rotor rotational momentum caused by variations in atmospheric density at different altitudes under crosswind conditions.

Table 3: Wilcoxon nonparametric tests for paired samples of false wind velocity signals between 30 m and 1000 m flight altitudes.

Wind Types	False Wind Signal	Significance	α	Test results
Tailwind/Headwind	$\Delta u_x^{T/HW}$	0.93	0.05	No difference
	$\Delta u_y^{T/HW}$	0.72	0.05	No difference
	$\Delta u_z^{T/HW}$	0.21	0.05	No difference
Crosswind	Δu_x^{CW}	0.36	0.05	No difference
	Δu_y^{CW}	0.00	0.05	Significant difference
	Δu_z^{CW}	0.81	0.05	No difference

3.3 Rotor Interference on Anemometer Measurements

This study employs a regression fitting to explore the relationship between the false wind signals generated by the UAV rotors airflow and the UAV's airspeed. Under tailwind and headwind conditions, the false wind signals ($\Delta u_x^{T/HW}$, $\Delta u_y^{T/HW}$, and $\Delta u_z^{T/HW}$) on the anemometer resulting from the UAV rotor -induced flows at both flight altitudes were aggregated and fitted as dependent variables in a regression using u_{x_sensor} as the independent variable. As shown in Fig. 8 (a), (b) and (c), good linear relationships were found between $\Delta u_x^{T/HW}$, $\Delta u_y^{T/HW}$, and $\Delta u_z^{T/HW}$ and the simulated velocity

353   components in the x-direction (u_{x_sensor}), respectively. The specific relationship is described by Eqs.

354   (12) to (14). Thus, using the UAV velocity components in x direction, the false wind signals caused by

355   the UAV propellers can be determined and removed from the raw measured wind velocity from the

356   anemometer.

357   For crosswind conditions, regressions were fitted with false wind signals (Δu_x^{CW} and Δu_z^{CW}) as

358   dependent variables and u_{x_sensor} as the independent variable in the same way (See Fig. 9). A linear

359   relationship was observed between the false wind signals in both x and z directions (Δu_x^{CW} and Δu_z^{CW})

360   and u_{x_sensor}, with the specific expressions in Eq. (15) and (16), respectively. As described in Sect. 3.2,

361   Δu_y^{CW} was sensitive to flight altitude under crosswind conditions, hence Δu_y^{CW} at 30 m and 1000 m

362   altitude ($\Delta u_{y(30)}^{CW}$ and $\Delta u_{y(1000)}^{CW}$) were regressed against u_{y_sensor} for the two flight altitudes

363   separately. The $\Delta u_{y(30)}^{CW}$ exhibited a linear relationship with u_{y_sensor}, as shown in Eq. (17). However,

364   the correlation coefficient between $\Delta u_{y(1000)}^{CW}$ and u_{y_sensor} was found to be lower than 0.5, indicating

365   that $\Delta u_{y(1000)}^{CW}$ may be considered independent of u_{y_sensor}. Therefore, the average value of $\Delta u_{y(1000)}^{CW}$

366   (0.006 m s^{-1}) was regarded as the $\Delta u_{y(1000)}^{CW}$ at this flight altitude.

367   Despite the dependence of Δu_y^{CW} on flight altitudes, $\Delta u_{y(30)}^{CW}$ and $\Delta u_{y(1000)}^{CW}$ are confined to a

368   similar numeric range. Therefore, they may be roughly considered as representing Δu_y for lower

369   altitude (e.g., 0 to 500 m) and higher altitude (e.g., 500 to 1000 m), respectively.

370   Hence, for crosswind situations, the wind velocities in the x, y and z directions measured by the

371   anemometer are corrected by subtracting Δu_x^{CW}, Δu_z^{CW} and $\Delta u_{y(0-500)}^{CW}$ which are estimated from

372     $u_{x\_sensor}/u_{y\_sensor}$, or at relatively high flight altitudes using a constant value of 0.006 m s^{-1} for

373     $\Delta u_{y(501-1000)}^{CW}$.

374
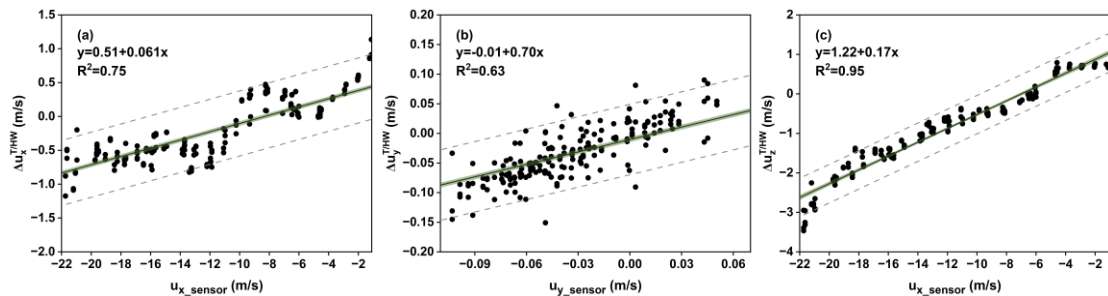
375 **Figure 8: Regression fit of artificial velocity ($\Delta u_x^{T/HW}$, $\Delta u_y^{T/HW}$ and $\Delta u_z^{T/HW}$) with u_{x_sensor} for tailwind and**

376 **headwind flight conditions at two altitudes. In the figure, simulation data are marked with black dots, fitted**

377 **curves are indicated in black lines, the 95% confidence bands are identified as green shadows, and the 95%**

378 **prediction bands are represented with gray dashed area.**

379
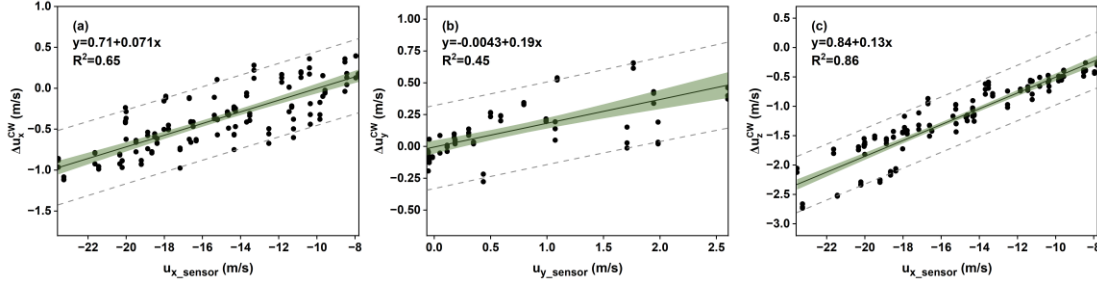
Figure 9: Regression fit of false wind velocity signals Δu_x^{CW}, Δu_z^{CW} and $\Delta u_{y(0-500)}^{CW}$ with $u_{x\_sensor}/u_{y\_sensor}$ for crosswind flight conditions at two altitudes. The symbols in the figure are the same as in Figure 6.

$$\Delta u_x^{T/HW} = 0.51 + 0.061 \times u_x, \tag{12}$$

$$\Delta u_y^{T/HW} = -0.01 + 0.70 \times u_y, \tag{13}$$

$$\Delta u_z^{T/HW} = 1.22 + 0.17 \times u_x, \tag{14}$$

$$\Delta u_x^{CW} = 0.71 + 0.071 \times u_x, \tag{15}$$

$$\Delta u_z^{CW} = 0.84 + 0.13 \times u_x, \tag{16}$$

$$\Delta u_{y(0-500)}^{CW} = -0.0043 + 0.19 \times u_y, \quad (h = 0 \sim 500 \text{ m}), \tag{17}$$

$$\Delta u_{y(501-1000)}^{CW} = 0.006, \quad (h = 501 \sim 1000 \text{ m}), \tag{18}$$

In Eq. (17) and (18), the variable h represents the flight altitude of the UAV.

3.4 The Overall Correction Algorithm

3.4.1 Motion and Attitude Compensation Correction of UAV

In addition to the false wind signals caused by propeller rotations, additional false wind velocity signals from the anemometer can be attributed to UAV movement and attitude (pitch, roll and yaw) changes during flight, and as such also need correction. When the UAV moves horizontally and vertically relative to the ground, the velocity vector measured by the anemometer is a vector combination of the true wind velocity and the UAV's ground velocity. Consequently, the ground velocity of the UAV (v_x and v_z, with v_y always 0 due to no motion in the y direction) contributes false wind velocity components to measurements by the anemometer. Moreover, the UAV's flight attitude undergoes adjustments in the pitch, roll, and yaw Euler angles (θ, φ, and ψ, respectively), in order to compensate for aerodynamic resistance or adapt to flight plans. These adjustments lead to the anemometer measuring additional velocities resulting from the rotational rates of the attitude angles ($\mu(\theta)$ and $\mu(\varphi)$, with $\mu(\psi)$ remaining zero due to the alignment of the rotational axis of ψ with the line connecting the UAV's center of gravity and the anemometer. Furthermore, the effect is further amplified by the distance (r) between

17

the anemometer and the UAV's center of gravity. It is noteworthy that there is currently no reported

correction algorithm for influence of attitude angle variations on anemometer wind velocity

measurements from UAVs. To obtain accurate wind information, after eliminating the aforementioned

interferences, the wind velocities (u_x, u_y and u_z) observed by the anemometer in the airframe coordinate

(x, y and z directions) were transformed to the North-East-Down (NED) ground coordinate using the

direction cosine matrix (DCM) as given in Eq. (19).

$$\begin{bmatrix} u_N \\ u_E \\ u_D \end{bmatrix} = \text{DCM}(\theta, \varphi, \psi) \left(\begin{bmatrix} u_x \\ u_y \\ u_z \end{bmatrix} + \begin{bmatrix} v_x \\ 0 \\ -v_z \end{bmatrix} + \begin{bmatrix} \mu(\theta) \\ -\mu(\varphi) \\ 0 \end{bmatrix} \right), \tag{19}$$

$$\text{DCM}(\theta, \varphi, \psi) = \begin{bmatrix} \cos(\psi) & -\sin(\psi) & 0 \\ \sin(\psi) & \cos(\psi) & 0 \\ 0 & 0 & 1 \end{bmatrix} \begin{bmatrix} \cos(\theta) & 0 & \sin(\theta) \\ 0 & 1 & 0 \\ -\sin(\theta) & 0 & \cos(\theta) \end{bmatrix} \begin{bmatrix} 1 & 0 & 0 \\ 0 & \cos(\varphi) & -\sin(\varphi) \\ 0 & \sin(\varphi) & \cos(\varphi) \end{bmatrix}, \tag{20}$$

where DCM is defined by Eq. (20); u_N, u_E and u_D refer to corrected North, East and Down

components of wind velocity in the ground coordinate; v_x and v_z are the motion velocities of the UAV

in the x and z directions respectively, which are directly provided by the GPS receiver output of the

UAV or can be directly computed from the UAV longitude/latitude coordinate output; $\mu(\theta)$ and $\mu(\varphi)$

represent the product of the pitch rate $\omega(\theta)$ and roll rate $\omega(\varphi)$, respectively, with the rotation radius r,

which is the distance between the anemometer and the center of gravity of the UAV, as defined in Eqs.

(21) and (22). Due to the alignment of the anemometer's z-axis with that of the UAV, the variation in

yaw ψ does not introduce false wind speed to signals from the anemometer in the airframe coordinate,

resulting in μ(ψ) being equal to zero.

$$\mu(\theta) = \omega(\theta) \times r = \frac{d(\theta)}{dt} \times r, \tag{21}$$

$$\mu(\varphi) = \omega(\varphi) \times r = \frac{d(\varphi)}{dt} \times r, \tag{22}$$

where $\omega(\theta)$ and $\omega(\varphi)$ are defined as the differentiation of θ and φ with respect to time t,

respectively.

3.4.2 Compensation Correction for Induced-Flow Disturbance by UAV Rotors

Based on the statistical analyses of the fluid simulation results in Sect. 3.3, the regression

relationships between the false wind velocity signals generated by the propeller rotation and the

simulated wind components sensed by the anemometer are integrated into the motion and attitude

18

429 correction algorithm of UAV given in Eq. (19). The updated wind velocity correction algorithm is given

430 as Eq. (23), whose second and third vectors on the right side of Eq. (23) represent the contributions of

431 the propeller-induced wind signals under tailwind/headwind and crosswind conditions to u_x, u_y and u_z,

432 respectively, with A and B defined in Eqs. (24) and (25) to quantify their magnitudes. Since the measured

433 wind velocities u_x and u_y from the anemometer correspond to the simulated u_{x_sensor} and u_{y_sensor},

434 respectively, the regression relationships are modified by replacing u_x and u_y with u_{x_sensor} and u_{y_sensor},

435 respectively. This yields the estimations of the false wind velocity signals, Δu_x, Δu_y and Δu_z, under

436 different wind directions, in relation to u_x and u_y, as specified by Eqs. (12) - (18). Using Eq. 16, the actual

437 wind velocity components, including north wind (u_N), east wind (u_E), and vertical wind (u_D), are

438 computed after correcting for the effects of UAV's rotor propeller disturbance, motion, and attitude on

439 the wind signal measurements from the anemometer.

440
$$
\begin{bmatrix} u_N \\ u_E \\ u_D \end{bmatrix} = \mathrm{DCM}(\theta, \varphi, \psi) \left(\begin{bmatrix} u_x \\ u_y \\ u_z \end{bmatrix} - \begin{bmatrix} A \times \Delta u_x^{T/HW} \\ A \times \Delta u_y^{T/HW} \\ A \times \Delta u_z^{T/HW} \end{bmatrix} - \begin{bmatrix} B \times \Delta u_x^{CW} \\ B \times \Delta u_y^{CW} \\ B \times \Delta u_z^{CW} \end{bmatrix} + \begin{bmatrix} v_x \\ 0 \\ v_z \end{bmatrix} + \begin{bmatrix} -\mu(\theta) \\ \mu(\varphi) \\ 0 \end{bmatrix} \right) ,
$$

441
(23)

442
$$
A = \left| \frac{u_x}{\sqrt{u_x{}^2 + u_y{}^2}} \right|,
$$
(24)

443
$$
B = \left| \frac{u_y}{\sqrt{u_x{}^2 + u_y{}^2}} \right|,
$$
(25)

444 **3.5 Validation of the Correction Algorithm**

445 A comparative experiment was designed to verify the effectiveness of the correction algorithm

446 described in Eq. (23). The experiment primarily compares three different wind data: the first is the three-

447 dimensional wind vector corrected only for UAV motion and attitude compensation (Eq. (19) and

448 denoted as $\mathbf{V_O}$), the second includes additional corrections for UAV rotor interference, along with motion

449 and attitude compensation (Eq. (23) and denoted as $\mathbf{V_R}$), and the third is the three-dimensional wind

450 directly measured by the meteorological tower (denoted as $\mathbf{V_T}$). The comparison experiment was

451 conducted with the UAV flying wind-boxes around the 80-meter meteorological tower within the

452 Experimental Base of the Beijing Key Laboratory of Cloud, Precipitation and Atmospheric Water

453 Resources. The meteorological tower was equipped with three-dimensional ultrasonic anemometers

454 positioned at heights of 30, 50, and 70 m, with one anemometer in the north and one in the south (see

455 Fig. 10). Experiments were conducted during the daytime on July 19, 2022, with neutral atmospheric

456 stability to minimize thermal boundary layer effects on vertical wind variability.

457 The UAV flew around the tower in a box flight path at a horizontal distance of about 10 m away

458 from the tower, at all three heights. During these flights, the UAV maintained a commanded horizontal

459 speed of approximately 5 m/s, a value selected as a compromise between achieving sufficient spatial

460 sampling resolution and maintaining stable flight attitude control. A total of 30 independent wind-box

461 flights were conducted, with each altitude (30, 50 m and 70 m) sampled 10 times. Each flight lasted

462 approximately 13 minutes, generating over 800 valid data points per altitude. Given the potential

463 interference from near-surface vegetation on the 30-meter anemometer on the tower, wind velocities

464 acquired by the UAV at 50 and 70 m heights during steady flight intervals were analyzed herein. Using

465 a 3σ threshold of the mean value of the entire dataset to exclude data outliers caused by sudden gusts

466 or UAV maneuvers (such as turning), retaining data during steady UAV flight periods.
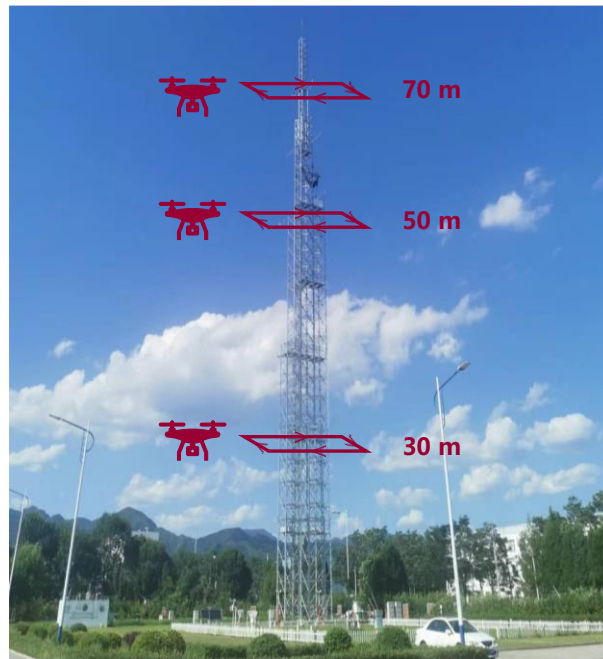

467
468 **Figure 10: Comparative experiment on wind measurements between the UAV and the meteorological tower.**

469 Fig. 11 presents the V_O, V_R, and V_T time-series data acquired during the dual-altitude flight tests

470 of the UAV at 70 m and 50 m, with the 70 m altitude test data collected prior to 15:05 and the 50 m

471 altitude test data obtained after 15:10. The results in Fig. 11 (a) demonstrate that at elevated wind speeds

472 (> 3 m s^{-1}), the wind velocities of V_R were substantially lower than that of V_O. The root mean square

473 relative errors between V_R and V_T, and V_O and V_T, are 0.28 and 0.37, respectively, with the former being

20

474 approximately 24% smaller than the latter. This indicates that the correction effect of Eq. (23) is

475 especially pronounced in strong wind conditions. In contrast, under gentle wind speeds ($\leqslant$ 3 m s^{-1}), $\mathbf{V_R}$

476 exhibited greater consistency with $\mathbf{V_O}$ but there was still a significant down-revision in the average speed

477 in $\mathbf{V_R}$. The average wind speeds of $\mathbf{V_O}$, $\mathbf{V_R}$, and $\mathbf{V_T}$ were 2.4, 1.91, and 1.81 m s^{-1}, respectively, with $\mathbf{V_R}$

478 exhibiting a 22% decrease compared to $\mathbf{V_O}$. The statistical analysis using the Wilcoxon signed-rank test

479 confirmed a significant difference ($p < 0.01$) in wind speed between $\mathbf{V_O}$ and $\mathbf{V_T}$, whereas no significant

480 differences ($p > 0.01$) were found between $\mathbf{V_R}$ and $\mathbf{V_T}$. This suggests that after compensating for UAV

481 motion, attitude, and rotor interference, the wind speed measured by the UAV anemometer is more

482 closely aligned with that measured directly by the meteorological tower. Moreover, under stronger winds,

483 the wind direction values of $\mathbf{V_R}$, $\mathbf{V_O}$, and $\mathbf{V_T}$ were relatively similar, yet at weaker winds, $\mathbf{V_R}$ showed a

484 small low-bias of about 3.3% (Fig. 11 (b)). The mediocre performance of $\mathbf{V_R}$ under low wind speeds

485 may originate from the disruption of stable maneuverability in drone rotors caused by low wind speeds,

486 which in turn leads to the failure of the correction algorithm based on CFD steady-state simulations.

487 Fig. 12 presents the wind rose diagrams, offering a detailed overview of the wind speed and

488 direction characteristics for $\mathbf{V_R}$, $\mathbf{V_O}$, and $\mathbf{V_T}$. Compared to the prevailing wind direction frequency (north

489 wind, 39%) of $\mathbf{V_T}$, the dominant wind direction frequency errors for $\mathbf{V_O}$ and $\mathbf{V_R}$ are 40% and 5%

490 respectively, demonstrating the superiority of $\mathbf{V_R}$ in correcting the prevailing wind direction frequency.

491 Meanwhile, deviations in the secondary components introduced by $\mathbf{V_R}$ (e.g., northwester wind) indicate

492 directions for subsequent model optimization. These analyses indicated that Eq. (23) can effectively

493 correct wind measurement biases induced by UAV disturbances, motion, and attitude changes,

494 particularly at higher wind speeds.

495 In addition, it should be emphasized that while this study primarily relied on meteorological tower

496 data for algorithm validation, cross-validation through industrial emission scenarios has further

497 confirmed the algorithm's robustness in complex flow fields (Han et al., 2023).

498
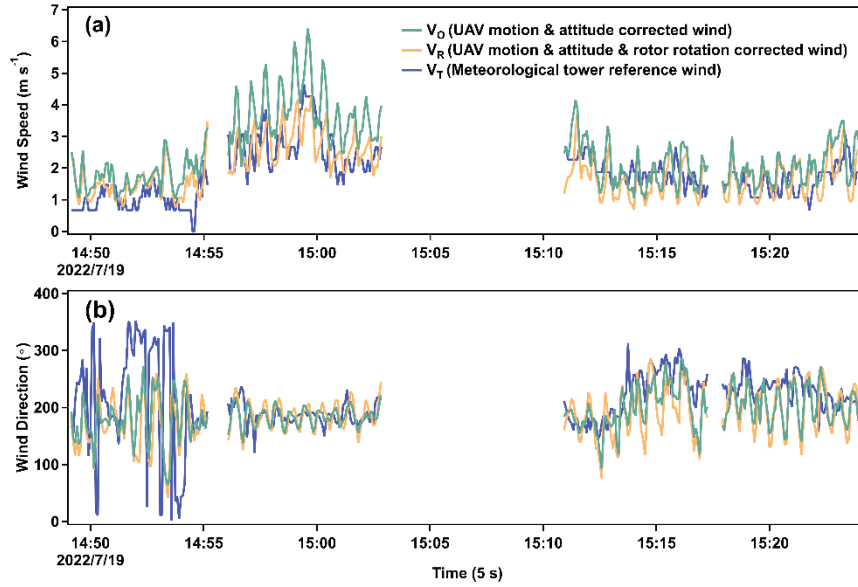
Figure 11: Comparison of wind speed and wind direction time series for V_R, V_O, and V_T. (a) Comparison of wind speed time series for V_R, V_O, and V_T. (b) Comparison of wind direction time series for V_R, V_O, and V_T. (Note: The meteorological tower measured wind data at 5 s intervals, while the UAV-based measured and corrected wind data were processed with a 10 s sliding average to suppress rotor-induced high-frequency noise, followed by 5 s non-overlapping averaging to align temporally with the tower's 5 s output interval.)

504
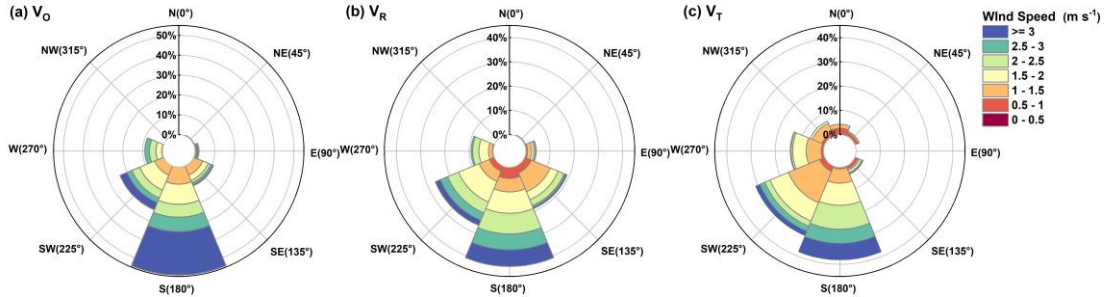
Figure 12: Comparison of wind roses for V_O, V_R, and V_T.

3.6 Discussion on the Limitations of the Algorithm

The current development of algorithms based on idealized steady-state CFD simulations relies on two key assumptions: low environmental turbulence intensity (0.1%) and turbulence length scales dominated by anemometer geometric parameters (0.012 meters). While this idealized setup effectively isolates rotor-induced flow distortion, its turbulence characteristics fundamentally differ from natural atmospheric conditions. However, it is crucial to emphasize that the algorithm's applicability under turbulent conditions remains valid. This is because rotor-induced wind speed deviations exhibit systemic long-time-scale characteristics, whereas atmospheric turbulence primarily affects measurement accuracy through random fluctuations in wind speed and direction with instantaneous nature. This

temporal-scale distinction enables our correction algorithm to effectively eliminate systemic biases while minimizing the impact of transient turbulence effects. Nevertheless, it should be noted that under stable atmospheric conditions (low wind speeds) as discussed in Sec. 3.5 or extreme weather scenarios, such airflow environments may disrupt the stable manoeuvrability of UAV rotors or obscure the systemic drainage effects of rotors, potentially leading to a nonlinear degradation in algorithm accuracy.

In addition, another limitation of our study is the assumption of a smooth surface in CFD simulations, which does not fully capture the impact of surface roughness on wind speed variations near the ground. In reality, surface roughness elements (e.g., vegetation, buildings, or terrain irregularities) alter the wind profile, increasing turbulence and wind shear in the atmospheric surface layer. This effect is particularly relevant for UAV-based wind measurements at low altitudes.

To further enhance the correction algorithm's applicability under diverse environmental conditions, future research will focus on the following aspects: conducting sensitivity studies under different turbulence intensity conditions, implementing supplementary correction modules specifically targeting atmospheric turbulence, and incorporating surface roughness length parameters in future CFD simulations. Although atmospheric turbulence presents significant challenges for UAV-based wind measurements, the correction framework established in this study has demonstrated its effectiveness in improving measurement accuracy across diverse meteorological conditions, thereby laying a critical foundation for developing reliable UAV-based wind measurement systems.

4 Conclusions

The scenarios involving direct measurements of wind fields within the atmospheric boundary layer using multirotor UAVs have become progressively commonplace, heightening the significance of accurate wind assessment. However, the rotor propellers during UAV flight introduce additional induced flows at the anemometer location, leading to false wind speed signals. For the present UAV-anemometer-payload configuration, a CFD-based method was used to simulate the process of the UAV wind measurement platform during stable flights under headwind, tailwind, and crosswind conditions. The analyses of induced airflows surrounding the anemometer led to a predictive tool for disturbance airflows. Building upon the UAV motion and attitude correction algorithm, a correction algorithm was proposed for the combined false wind signals from UAV rotor propeller disturbance, motion, and attitude

changes during UAV flights. Through comparison of the corrected wind speeds derived from measurements taken from the UAV platform and concurrent three-dimensional wind measurements from a nearby meteorological tower, the validity of the correction algorithm has been demonstrated. Although the algorithm still has certain limitations, it provides a feasible approach for the direct measurement of wind speed from multirotor UAV flights.

In conclusion, this study represents a significant advancement in three-dimensional wind speed measurement using UAV platforms, presenting a practical and effective method for direct and accurate wind measurement. This technological breakthrough not only creates a strong foundation for precise wind field measurements with UAVs but also provides potential avenues for the accurate quantification of gaseous pollutant emissions based on UAV. The outcomes of this work carry considerable scientific importance and offer valuable practical applications.

Data availability. Data are available from the corresponding author upon reasonable request.

Author contributions. YY conducted CFD simulations, performed data analysis, and drafted the initial manuscript. YZ contributed to the development of calibration algorithms and provided algorithm programming. YY and TH designed and conducted flight measurement validation experiments under the guidance of SML. DZ provided the site for the flight measurement validation experiments. CX, YL, and YH assisted in refining simulation scenarios and algorithms. JZ, HS, and KZ contributed to the improvement of data analysis methods. SML reviewed and edited the manuscript to ensure the accuracy and completeness of the research.

Competing interest. The contact author has declared that none of the authors has any competing interests.

Reference

Afaq, M. and Ahmad, R.: Comparison Between ANSYS Fluent and Solidworks Internal Flow

Simulation for Analysis of A Fuzzy Logic Controller-Based Heating/Cooling System in A Mobile Robot Design, In: 2023 International Conference on Robotics and Automation in Industry (ICRAI), IEEE, 1-6, 10.1109/ICRAI57502.2023.10089571, 2023.

Anderson, K. and Gaston, K. J.: Lightweight unmanned aerial vehicles will revolutionize spatial ecology, Front. Ecol. Environ., 11, 138-146, https://doi.org/10.1890/120150, 2013.

Azmi, M. F. M., Marzuki, M. A. B., and Bakar, M. A. A.: Vehicle aerodynamics analysis of a multi-purpose vehicle using CFD, ARPN Journal of Engineering and Applied Sciences, 12, 2345-2350, 2017.Barbieri, L., Kral, S. T., Bailey, S. C. C., Frazier, A. E., Jacob, J. D., Reuder, J., Brus, D., Chilson, P. B., Crick, C., Detweiler, C., Doddi, A., Elston, J., Foroutan, H., Gonzalez-Rocha, J., Greene, B. R., Guzman, M. I., Houston, A. L., Islam, A., Kemppinen, O., Lawrence, D., Pillar-Little, E. A., Ross, S. D., Sama, M. P., Schmale, D. G., Schuyler, T. J., Shankar, A., Smith, S. W., Waugh, S., Dixon, C., Borenstein, S., and de Boer, G.: Intercomparison of small unmanned aircraft system (sUAS) measurements for atmospheric science during the LAPSE-RATE campaign, Sensors (Basel), 19, https://doi.org/10.3390/s19092179, 2019.Bonin, T. A., Chilson, P. B., Zielke, B. S., Klein, P. M., and Leeman, J. R.: Comparison and application of wind retrieval algorithms for small unmanned aerial systems, Geosci. Instrum., Methods Data Syst., 2, 177-187, https://doi.org/10.5194/gi-2-177-2013, 2013.

Booij, N., Ris, R. C., and Holthuijsen, L. H.: A third-generation wave model for coastal regions: 1. Model description and validation, J. Geophys. Res.: Oceans, 104, 7649-7666, https://doi.org/10.1029/98JC02622, 1999.

Crowe, D., Pamula, R., Cheung, H. Y., and De Wekker, S. F.: Two supervised machine learning approaches for wind velocity estimation using multi-rotor copter attitude measurements, Sensors, 20, 5638, https://doi.org/10.3390/s20195638, 2020.

de Divitiis, N.: Wind estimation on a lightweight vertical-takeoff- and-landing uninhabited vehicle, J. Aircr., 40, 759-767, https://doi.org/10.2514/2.3155, 2003.

Dao, M. H., Zhang, B., Xing, X., Lou, J., Tan, W. S., Cui, Y., and Khoo, B. C.: Wind tunnel and CFD studies of wind loadings on topsides of offshore structures, Ocean Eng., 285, 115310, https://doi.org/10.1016/j.oceaneng.2023.115310, 2023.

Donnell, G. W., Feight, J. A., Lannan, N., and Jacob, J. D.: Wind characterization using onboard IMU of sUAS, In: 2018 Atmospheric flight mechanics conference, 2986, https://doi.org/10.2514/6.2018-2986,

2018.Drob, D. P., Emmert, J. T., Meriwether, J. W., Makela, J. J., Doornbos, E., Conde, M., Hernandez, G., Noto, J., Zawdie, K. A., McDonald, S. E., Huba, J. D., and Klenzing, J. H.: An update to the Horizontal Wind Model (HWM): The quiet time thermosphere, Earth Space Sci., 2, 301-319, https://doi.org/10.1002/2014EA000089, 2015.

Elston, J., Argrow, B., Stachura, M., Weibel, D., Lawrence, D., and Pope, D.: Overview of small fixed-wing unmanned aircraft for meteorological sampling, J. Atmos. Ocean. Technol., 32, 97-115, https://doi.org/10.1175/Jtech-D-13-00236.1, 2015.

Gonzalez-Rocha, J., Woolsey, C. A., Sultan, C., and De Wekker, S. F. J.: Sensing wind from quadrotor motion, J. Guid. Control Dyn., 42, 836-852, https://doi.org/10.2514/1.G003542, 2019.

Gousseau, P., Blocken, B., Stathopoulos, T., and van Heijst, G. J. F.: CFD simulation of near-field pollutant dispersion on a high-resolution grid: A case study by LES and RANS for a building group in downtown Montreal, Atmos. Environ., 45, 428-438, https://doi.org/10.1016/j.atmosenv.2010.09.065, 2011.

Gryning, S. E., Holtslag, A. A. M., Irwin, J. S., and Sivertsen, B.: Applied dispersion modelling based on meteorological scaling parameters, Atmos. Environ., 21, 79-89, https://doi.org/10.1016/0004-6981(87)90273-3, 1987.

Haleem, A.: Vehicular Aerodynamics Wind Tunnel Testing of Unmanned Aerial Multirotor Vehicles and Wall Interference Corrections, PhD Thesis, Toronto Metropolitan University, 2021.

Han T, X. C., Liu Y, Yang Y, Zhang Y, Huang Y, Gao X, Zhang X., Bao F, and Li S-M.: Application of a new UAV measurement methodology to the quantification of CO_{-2} and CH_4 emissions from a major coking plant, Atmos. Meas. Tech., 1-21, https://doi.org/10.5194/amt-17-677-2024, 2023.

Hedworth, H., Page, J., Sohl, J., and Saad, T.: Investigating Errors Observed during UAV-Based Vertical Measurements Using Computational Fluid Dynamics, Drones, 6, 253, https://doi.org/10.3390/drones6090253, 2022.

Hoang, M. L., Carratu, M., Paciello, V., and Pietrosanto, A.: Noise Attenuation on IMU Measurement For Drone Balance by Sensor Fusion, in: 2021 IEEE International Instrumentation and Measurement Technology Conference (I2MTC), 1-6, https://doi.org/10.1109/i2mtc50364.2021.9460041, 2021.

Johansen, T. A., Cristofaro, A., Sorensen, K., Hansen, J. M., and Fossen, T. I.: On estimation of wind velocity, angle-of-attack and sideslip angle of small UAVs using standard sensors, in: 2015 International

Conference on Unmanned Aircraft Systems (ICUAS), 510-519, https://doi.org/10.1109/icuas.2015.7152330, 2015.

Jonuskaite, A.: Flow simulation with SolidWorks, 2017.

Kim, M.-S. and Kwon, B. H.: Estimation of sensible heat flux and atmospheric boundary layer height using an unmanned aerial vehicle, Atmosphere, 10, 363, https://doi.org/10.3390/atmos10070363, 2019.

Langelaan, J. W., Alley, N., and Neidhoefer, J.: Wind field estimation for small unmanned aerial vehicles, J. Guid. Control Dyn., 34, 1016-1030, https://doi.org/10.2514/1.52532, 2011.

Martin, S., Bange, J., and Beyrich, F.: Meteorological profiling of the lower troposphere using the research UAV "M^{2}AV Carolo", Atmos. Meas. Tech., 4, 705-716, https://doi.org/10.5194/amt-4-705-2011, 2011.

McGonigle, A., Aiuppa, A., Giudice, G., Tamburello, G., Hodson, A., and Gurrieri, S.: Unmanned aerial vehicle measurements of volcanic carbon dioxide fluxes, Geophys. Res. Lett., 35, https://doi.org/10.1029/2007GL032508, 2008.

Neumann, P. P. and Bartholmai, M.: Real-time wind estimation on a micro unmanned aerial vehicle using its inertial measurement unit, Sens. Actuators, A, 235, 300-310, https://doi.org/10.1016/j.sna.2015.09.036, 2015.

Niedzielski, T., Skjøth, C., Werner, M., Spallek, W., Witek, M., Sawiński, T., Drzeniecka-Osiadacz, A., Korzystka-Muskała, M., Muskała, P., and Modzel, P.: Are estimates of wind characteristics based on measurements with Pitot tubes and GNSS receivers mounted on consumer-grade unmanned aerial vehicles applicable in meteorological studies?, Environ. Monit. Assess., 189, 1-18, https://doi.org/10.1007/s10661-017-6141-x, 2017.

Nolan, P. J., Pinto, J., Gonzalez-Rocha, J., Jensen, A., Vezzi, C. N., Bailey, S. C. C., de Boer, G., Diehl, C., Laurence, R., Powers, C. W., Foroutan, H., Ross, S. D., and Schmale, D. G.: Coordinated unmanned aircraft system (UAS) and ground-based weather measurements to predict Lagrangian coherent structures (LCSs), Sensors (Basel), 18, https://doi.org/10.3390/s18124448, 2018.

Oktay, T. and Eraslan, Y.: Computational fluid dynamics (Cfd) investigation of a quadrotor UAV propeller, International Conference on Energy, Environment and Storage of Energy, 21-25,

Palomaki, R. T., Rose, N. T., van den Bossche, M., Sherman, T. J., and De Wekker, S. F.: Wind estimation in the lower atmosphere using multirotor aircraft, J. Atmos. Ocean. Technol., 34, 1183-1191,

https://doi.org/10.1175/JTECH-D-16-0177.1, 2017.

Pettersson, K. and Rizzi, A.: Aerodynamic scaling to free flight conditions: Past and present, Prog. Aerosp. Sci., 44, 295-313, https://doi.org/10.1016/j.paerosci.2008.03.002, 2008.

Quan, Q.: Introduction to Multicopter Design and Control, Springer Singapore, 384 pp., https://doi.org/10.1007/978-981-10-3382-7, 2017.

Ramya, P., Kumar, A. H., Moturi, J., and Ramanaiah, N.: Analysis of flow over passenger cars using computational fluid dynamics, Int J Eng Trends Technol (IJETT), 29, 170-176, 10.14445/22315381/IJETT-V29P232 2015.

Rautenberg, A., Graf, M. S., Wildmann, N., Platis, A., and Bange, J.: Reviewing wind measurement approaches for fixed-wing unmanned aircraft, Atmosphere, 9, https://doi.org/10.3390/atmos9110422, 2018.

Riddell, K. D. A.: Design, testing and demonstration of a small unmanned aircraft system (SUAS) and payload for measuring wind speed and particulate matter in the atmospheric boundary layer, University of Lethbridge, Canada, 2014.

Rogers, K. and Finn, A.: Three-dimensional UAV-based atmospheric tomography, J. Atmos. Ocean. Technol., 30, 336-344, https://doi.org/10.1175/JTECH-D-12-00036.1, 2013.

Seibert, P., Beyrich, F., Gryning, S. E., Joffre, S., Rasmussen, A., and Tercier, P.: Review and intercomparison of operational methods for the determination of the mixing height, Atmos. Environ., 34, 1001-1027, https://doi.org/10.1016/S1352-2310(99)00349-0, 2000.

Shaw, J. T., Shah, A. D., Yong, H., and Allen, G.: Methods for quantifying methane emissions using unmanned aerial vehicles: a review, Philos. T. Roy. Soc. A, 379, https://doi.org/10.1098/rsta.2020.0450, 2021.

Shimura, T., Inoue, M., Tsujimoto, H., Sasaki, K., and Iguchi, M.: Estimation of wind vector profile using a hexarotor unmanned aerial vehicle and its application to meteorological observation up to 1000 m above surface, J. Atmos. Ocean. Technol., 35, 1621-1631, https://doi.org/10.1175/JTECH-D-17-0186.1, 2018.

Sikkel, L., de Croon, G., De Wagter, C., and Chu, Q.: A novel online model-based wind estimation approach for quadrotor micro air vehicles using low cost MEMS IMUs, In: 2016 IEEE/RSJ International Conference on Intelligent Robots and Systems (IROS), IEEE, 2141-2146, 10.1109/IROS.2016.7759336,

685 2016.

686 Simma, M., Mjøen, H., and Boström, T.: Measuring wind speed using the internal stabilization system

687 of a quadrotor drone, Drones, 4, 23, https://doi.org/10.3390/drones4020023, 2020.

688 Soddell, J. R., McGuffie, K., and Holland, G. J.: Intercomparison of atmospheric soundings from the

689 Aerosonde and radiosonde, J. Appl. Meteorol., 43, 1260-1269, https://doi.org/10.1175/1520-

690 0450(2004)043<1260:IOASFT>2.0.CO;2, 2004.

691 Spiess, T., Bange, J., Buschmann, M., and Vorsmann, P.: First application of the meteorological Mini-

692 UAV 'M^{2}AV', Meteorol. Z., 16, 159-170, https://doi.org/10.1127/0941-2948/2007/0195, 2007.

693 Stewart, M., Martin, S., and Barrera, N., Barrera, N. (Ed.): Unmanned aerial vehicles: fundamentals,

694 components, mechanics, and regulations, Unmanned Aerial Vehicles, Nova Science Publishers,

695 Hauppauge, New York, USA, 71 pp.2021.

696 Stockie, J. M.: The mathematics of atmospheric dispersion modeling, SIAM Rev., 53, 349-372,

697 https://doi.org/10.1137/10080991X, 2011.

698 Thielicke, W., Hubert, W., Muller, U., Eggert, M., and Wilhelm, P.: Towards accurate and practical

699 drone-based wind measurements with an ultrasonic anemometer, Atmos. Meas. Tech., 14, 1303-1318,

700 https://doi.org/10.5194/amt-14-1303-2021, 2021.

701 van Hooff, T. and Blocken, B.: Coupled urban wind flow and indoor natural ventilation modelling on a

702 high-resolution grid: A case study for the Amsterdam ArenA stadium, Environ. Model. Softw., 25, 51-

703 65, https://doi.org/10.1016/j.envsoft.2009.07.008, 2010.

704 Vardoulakis, S., Fisher, B. E. A., Pericleous, K., and Gonzalez-Flesca, N.: Modelling air quality in street

705 canyons: a review, Atmos. Environ., 37, 155-182, https://doi.org/10.1016/S1352-2310(02)00857-9,

706 2003.

707 Villa, T. F., Gonzalez, F., Miljievic, B., Ristovski, Z. D., and Morawska, L.: An overview of small

708 unmanned aerial vehicles for air quality measurements: Present applications and future prospectives,

709 Sensors (Basel), 16, https://doi.org/10.3390/s16071072, 2016.

710 Yang, Y., Zhou, J., Xie, C., Tian, W., Xue, M., Han, T., Chen, K., Zhang, Y., Liu, Y., and Huang, Y.: A

711 New Methodology for High Spatiotemporal Resolution Measurements of Air Volatile Organic

712 Compounds: From Sampling to Data Deconvolution, Environ. Sci. Technol., 58, 12488-12497, 2024.

713